Structural Engineering and Mechanics, *Vol. 72, No. 2 (2019) 217-227*
DOI: https://doi.org/10.12989/sem.2019.72.2.217

Shape sensing with inverse finite element method for slender structures

Pierclaudio Savino*[1], Marco Gherlone[2a] and Francesco Tondolo[1b]

[1]*Department of Structural, Geotechnical and Building Engineering, Politecnico di Torino, Corso Duca degli Abruzzi 24, Torino, Italy*
[2]*Department of Mechanical and Aerospace Engineering, Politecnico di Torino, Corso Duca degli Abruzzi 24, Torino, Italy*

(Received February 25, 2019, Revised May 24, 2019, Accepted May 30, 2019)

Abstract. The methodology known as "shape sensing" allows the reconstruction of the displacement field of a structure starting from strain measurements, with considerable implications for structural monitoring, as well as for the control and implementation of smart structures. An approach to shape sensing is based on the inverse Finite Element Method (iFEM) that uses a variational principle enforcing a least-squares compatibility between measured and analytical strain measures. The structural response is reconstructed without the knowledge of the mechanical properties and load conditions but based only on the relationship between displacements and strains. In order to efficiently apply iFEM to the most common structural typologies of civil engineering, its formulation according to the kinematical assumptions of the Bernoulli-Euler theory is presented. Two beam inverse finite elements are formulated for different loading conditions. Depending on the type of element, the relationship between the minimum number of required measurement stations and the interpolation order is defined. Several examples representing common applications of civil engineering and involving beams and frames are presented. To simulate the experimental strain data at the station points and to verify the accuracy of the displacements obtained with the iFEM shape sensing procedure, a direct FEM analysis of the considered structures is performed using the LUSAS software.

Keywords: shape sensing; iFEM; Euler-Bernoulli theory; structural monitoring; displacements

1. Introduction

Aging is an unavoidable problem that negatively affects the structures performance since it begins as soon as they are into service. Preserving structures durability is a very important aspect that has environmental, social and economic impacts. In this context, Structural Health Monitoring (SHM), i.e., the continuous detection of health and residual life of a structure, allows to improve the efficiency of maintenance procedures, intervening only when it is strictly necessary also optimizing costs. However, SHM for civil buildings still faces many challenges. In fact, structures are usually larger, traditional sensors are point sensors that do not allow to identify the structural global behavior, traditional local inspections are laborious, expensive and are based on staff training, dynamic properties are influenced by environmental and usage conditions that vary over time, vibrational analyses require to store large volumes of data.

Nevertheless, the progress in materials technology, data acquisition, transmission and computational techniques has made the SHM a widely accepted technology for diagnosing and monitoring the state of structural health in the field of civil engineering (Serker and Wu 2010). The monitoring of structures based on strain measurements is one of the possible procedures. Known as shape sensing, this technique consists in the reconstruction of the displacement field of a structure starting from strain measurements in discrete points known as station points. The knowledge of the full displacement field has important implications for the structural health monitoring, as well as for the control and implementation of smart structures. In the last two decades, with the progress of silicon technology in reducing the cost of the sensing devices, a considerable number of investigations have been conducted for the development of various detection techniques and types of engineering structures.

In literature, a wide variety of new sensing technologies and SHM techniques are present. Zeng *et al*. (2002) performed a strain measurement of a reinforced concrete beam by means of optical fibers both embedded in glass-fiber reinforced polymer rods and directly bonded to the steel reinforcing bars. In the latter case the system provided accurate strain measurements whereas in epoxy-coated setup, in presence of high deformation gradients, lower strain readings were registered. In order to overcome or at least reduce this problem, several Authors have incorporated the optical fiber into the reinforcing bars. Ju *et al*. (2018) have introduced a smart reinforcing bar with fiber Bragg grating sensor made of glass fiber reinforced polymer. Experimental results have demonstrated that can be used as reinforcement of concrete member with strong advantages in terms of durability and smart monitoring. Quiertant *et al*. (2013) implemented optical fiber sensors in reinforcing bars for reinforced concrete deformation

*Corresponding author, Research assistant
E-mail: pierclaudio.savino@polito.it
[a] Professor
E-mail: marco.gherlone@polito.it
[b] Professor
E-mail: francesco.tondolo@polito.it

http://www.techno-press.com/journals/sem&subpage=7 ISSN: 1225-4568 (Print), 1598-6217 (Online)

measurements. It was verified that the embedded fiber optic offers a better strain transfer than the surface bonded fiber optic. Tondolo *et al*. (2018) provided a new concept of reinforced instrumented steel bar, named smart steel system, achieving strain sensing capabilities by incorporating a low-cost barometric pressure sensor within a hermetic cavity drilled into the bar. Villalba and Casas (2012) have experienced the possibility and accuracy of identifying the cracks in a reinforced concrete slab using fiber optic. The results show how the fiber optic sensor is not only capable to detect the appearance of cracks, but also to perform correctly the analysis up to high load levels producing a crack width in the range of 1 mm. Rodriguez *et al*. (2016) implemented a novel technique in partially pre-stressed concrete beams with optical fiber sensors in order to detect induced shear cracks. Henault *et al*. (2012) monitored the mechanical behavior of a reinforced concrete beam tested under four points loading test and instrumented with different optical fiber detection cables installed at various points. It has been found that the position of the sensors has little influence on the deformation measurements. Moreover, it was observed that, although the sample was severely damaged at high loads levels, the optical fiber systems were still efficient and provided strain values consistent with those of conventional reference sensors. Unsal *et al*. (2017) presented experimental results of continuous concrete beams reinforced with glass fiber reinforced polymer bars or reinforced also with steel bars. Good agreement has been found between experimental and theoretical results. At a larger scale, there are numerous examples of monitoring large structural systems. Shi *et al*. (2009) tested the feasibility of the application of Brilliouin Optical Time Domain Reflectometer sensing system for slopes engineering. The advantage of the system is the ability to continuously measure all points of the slope from one end of a sensitive optical fiber. Shi *et al*. (2003) tested the feasibility of applying optical fiber for strain measurement in the Taiwan Strait Tunnel project. Thévenaz *et al*. (1999) performed demonstration tests of distributed temperature and strain measurements using a tool based on local analysis of the stimulated Brillouin interaction for a dam. Zhu *et al*. (2009) computed the displacement profile of a dam according to the Bernoulli-Euler model and using the strain distribution measured by fiber Bragg grating sensing bar. Regier and Hoult (2014) investigated the performance of a distributed fiber optic strain measurement technology during a loading test on a reinforced concrete bridge. The strain measurements of the fiber optic sensors have been validated with those of the strain gauges presenting similar data trend. The results were then used to calculate the deflection and to compare it with the transducer measurements obtaining good results provided the boundary conditions are correctly defined.

In addition to the development of innovative technologies for various engineering applications, a progress from the computational point of view is registered. In particular, one of the best goals is to find an algorithm that allows to reconstruct the deformed shape of the entire structure using a very small number of measurement stations. Some methodologies that aim at reconstructing the entire displacement field are present in literature and involve the numerical integration of the experimental strains, the use of continuous basic functions to approximate the displacement field such as neural networks or a finite element discrete variational principle (Gherlone *et al*. 2018). Akl *et al*. (2007) proposed a method for wireless distributed detection of the deformed shape of a beam using the nonlinear finite element theory through the integration of the von Karman relation. Ko *et al*. (2009) developed and evaluated a strategy to detect the deformed shape of non-uniform beams. The displacement equations were formulated in terms of bending strains evaluated at multiple strain-sensing stations embedded on the surface of the beam. The measured bending strain data are then used by the displacement equations for the calculations of deflections and the cross-sectional twist angle. Glaser *et al*. (2012) presented a method based on the use of curvature measures to reconstruct the form and compare this method with the techniques using the position data. The method uses splines whose coefficients are estimated using continuity conditions, boundary conditions and measured bending estimates. Kirby *et al*. (1997) examined the approximation of the strain field of a cantilever beam using both linear and quadratic local basis functions. Kim and Ko (2004) applied classical beam equations to estimate continuously bending deformation by using measured strains. By regression analysis they reconstructed a strain function from the measured strain data. Jiang *et al*. (2018) proposed a new displacement time-series prediction model based on the neural network approach. Mao and Todd (2008) explored a simplified data-based neural network approach and model-based basis functions approach for reconstructing displacement. In the data-based linear neural network approach, the strain measurements are related with displacements by a simplified linear mapping obtained after training the system, whereas the model-based approach is based on basis function projections. It was found that the consistency between the type of training cases and the type of test cases affects the accuracy of reconstruction with neural networks. Particularly promising and versatile are the variational approaches, which employ different types of functional errors and involve finite elements to solve the inverse problem of the reconstruction of the full-field deformed shape. Shkarayev *et al*. (2001) developed a finite element methodology which involves an inverse formulation that employs strains measured on the surface to reconstruct the loads, stresses and displacements pattern. In particular, the load is approximated by a polynomial whose coefficients are evaluated through the least-squares minimization of calculated and measured strains. Many of the methods presented require knowledge of the loading conditions, of the mechanical properties of materials, data that are often difficult to detect without laboratory tests. For these reasons, such approaches are generally unsuitable for use in the SHM algorithm because a suitable algorithm should be general, robust, stable and precise in a wide range of loads, materials, inertial characteristics and inherent errors in deformation measurements, fast enough for real-time applications (Gherlone *et al*. 2012). An algorithm that seems to satisfy the above requirements was developed by Tessler and Spangler (2003). The methodology, called inverse Finite Element Method (iFEM), uses a minimized weighted variational principle and a discretization of continuous finite elements containing data from arbitrarily positioned and arbitrarily oriented strain sensors. Starting from the relationships between strains and displacements, without knowing the mechanical, inertial, load and damping properties, it is possible to reconstruct the static and dynamic response of a discretized structural domain in a stable and precise way. To arbitrarily model plates and shells, Tessler and Spangler (2004) created the inverse 3-node element called iMIN3 and based on Mindlin's theory. Several applications, assessment studies and enhancements of the original iFEM for plates and shells have been presented in the open literature. iMIN3 has been used by Cerracchio *et al*. (2015a) to perform shape-sensing on a multilayered stiffened panel subjected to thermo-mechanical loads and by Papa *et al*. (2017) to the displacements field reconstruction of a simplified fixed-wing structure for a UAS (Unmanned Aircraft System). A quadrilateral inverse shell element (iQS4) has been developed by Kefal *et al*. (2016a) and then applied to the shape sensing of a chemical tanker mid-ship and of a container ship (Kefal *et al*. 2016b, c). More recently, Kefal *et al*. (2018) have used iQS4 for the shape and stress monitoring of bulk carriers starting from strains measured with fiber-optic sensors and under the effect of measurement noise. The iFEM approach has been further extended to multilayered composite and sandwich plates by Cerracchio *et al*. (2015b) and by Kefal *et al*. (2017a, b). The iFEM procedure was specialized by Gherlone *et al*. (2008, 2012) for the shape sensing of truss, beam and frame structures instrumented with strain gauges. The kinematical hypotheses are those of shear deformation theory of Timoshenko that incorporates axial, bending, torsional and transverse shear deformations in three dimensions. The beam iFEM approach has been subsequently assessed by way of comparison with reference results coming from numerical models and experimental measurements by Gherlone *et al*. (2012, 2014).

The aim of the present work is to develop and implement for the first time the iFEM method under the kinematic assumptions of the Bernoulli-Euler theory in order to apply this methodology also for the most common case in civil engineering of slender structural elements. This hypothesis, generally efficient for the modeling of civil structures, also entails an advantage with respect to the original formulation by Gherlone *et al*. (2012) in terms of the number of input data needed, as will be shown in Section 5. The formulation uses the variational least squares principle used by Gherlone *et al*. (2012), which in this work involves axial deformation and curvatures. The variational formulation allows to discretize the structure using appropriate inverse beam finite elements. Depending on the desired interpolation degree, two inverse elements are presented, called 0th order element and 1st order element. A direct FEM analysis performed with the LUSAS code is used to simulate the sensor strain measurements. In the finite element analysis, a linear and elastic material behavior is assumed and both distributed and concentrated loading conditions are considered. Strain data generated by LUSAS are the inputs of the shape sensing reconstruction process, while the displacement data produced by LUSAS is used as reference results to evaluate the accuracy of the displacement estimated by the iFEM approach.

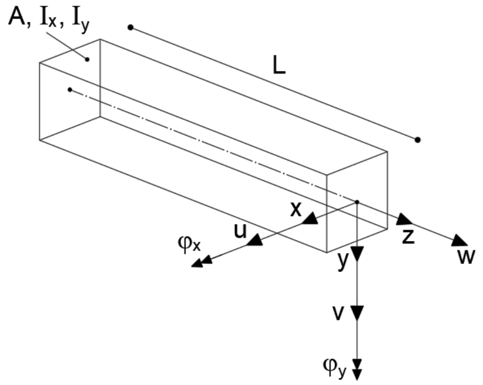

Fig. 1 Geometrical properties and kinematic parameters

2. Bernoulli-Euler beam theory

Consider a straight beam with constant cross-section, in the Cartesian reference system (x, y, z) as shown in Fig. 1. The reference system has the z axis coinciding with the longitudinal axis of the beam and the x and y axes are the section's principal axes of inertia.

The element of length L and section area A is characterized by the moments of inertia I_x and I_y referred, respectively, to the x and y axes.

The constituent material is elastic, homogeneous and isotropic with the following mechanical properties: E (Young's modulus), G (shear modulus) and (Poisson coefficient). Assuming that torsion does not occur, the kinematics of the beam in space is defined by the following displacement field

$$u_z(x,y,z) = w(z) + y \cdot \varphi_x(z) - x \cdot \varphi_y(z)$$
$$u_y(x,y,z) = v(z)$$
$$u_x(x,y,z) = u(z)$$

where u_x, u_y, u_z are the displacements in the x, y and z directions; w, v and u are the displacements of the section's centroid at the axial position z; φ_x and φ_y are the rotations around the x and y axis, respectively. The kinematic variables that describe the displacement field can be grouped in the vector

$$\mathbf{u} = \{w, v, \varphi_x, u, \varphi_y\}^T$$

The corresponding strain field deriving from the linear elastic theory results

$$\varepsilon_z(x,y,z) = w_{,z}(z) + y \cdot \varphi_{x,z}(z) - x \cdot \varphi_{y,z}(z)$$
$$\gamma_{zx}(z) = u_{,z}(z) - \varphi_y(z) = 0$$
$$\gamma_{zy}(z) = v_{,z}(z) + \varphi_x(z) = 0$$

According to the kinematical assumptions of Bernoulli-Euler theory, the deformed sections remains flat and orthogonal to the beam axis and for these reasons the transverse shear strains vanish. Therefore, the strain field is characterized by the only axial component

$$\varepsilon_z(x,y,z) = \varepsilon_{z0}(z) + y \cdot \chi_x(z) - x \cdot \chi_y(z)$$

where ε_{z0} is the axial strain, χ_x and χ_y are the curvatures related to the displacements from the relations

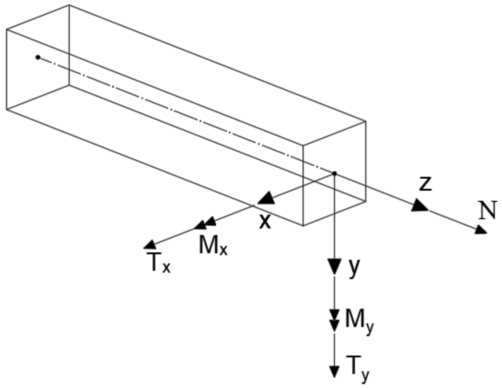

Fig. 2 Static characteristics

$$
\begin{aligned}
\varepsilon_{z0} &= \frac{dw}{dz} \\
\chi_x = \varphi_{x,z} &= -\frac{d^2 v}{dz^2} \\
\chi_y = \varphi_{y,z} &= \frac{d^2 u}{dz^2}
\end{aligned} \tag{1}
$$

The section strains that define the kinematic model are grouped in the vector

$$\mathbf{e}(\mathbf{u}) = \{\varepsilon_{z0}, \chi_x, \chi_y\}^T$$

From the constitutive equations, the resultant forces and moments (Fig. 2) are

$$
\begin{aligned}
N &= EA \cdot \varepsilon_{z0} \\
M_x &= EI_x \cdot \chi_x \\
M_y &= EI_y \cdot \chi_y
\end{aligned} \tag{2}
$$

where EA is the axial stiffness, EI_x and EI_y the bending stiffnesses.

In case of a beam subjected to distributed loads in the three directions $p_z(z)$, $q_y(z)$ and $q_x(z)$, the indefinite equilibrium equations of the beam are

$$
\begin{aligned}
\frac{dN}{dz} &= -p_z(z) \\
\frac{dT_y}{dz} &= -q_y(z) \\
\frac{dM_x}{dz} &= T_y \\
\frac{dT_x}{dz} &= -q_x(z) \\
\frac{dM_y}{dz} &= T_x
\end{aligned} \tag{3}
$$

3. Inverse Finite Element Method for the Bernoulli-Euler beam theory

To reconstruct the deformed shape of an element from strains measured in situ, the least squares functional $\Phi(u)$ is minimized with respect to the kinematic variables. Indicating with e(u) the analytical section strains related to the Bernoulli-Euler theory and with e the experimental section strains measured in situ, the functional results

$$\boldsymbol{\Phi}(\mathbf{u}) = \left|\left|\mathbf{e}(\mathbf{u}) - \mathbf{e}^{\varepsilon}\right|\right|^2$$

The kinematic variables are interpolated using appropriate shape functions N(z) of degree consistent with the behaviour of the beam

$$\mathbf{u}(z) = \mathbf{N}(z) \cdot \mathbf{u}^e \tag{4}$$

where u^e indicates the nodal degrees of freedom. In the case of discretization with m elements, the functional is equal to the sum of each element contribution

$$\boldsymbol{\Phi} = \sum_{e=1}^{m} \boldsymbol{\Phi}^e$$

With reference to axial strain and curvatures, the functional error to be minimized is defined as

$$
\begin{aligned}
\Phi_{\varepsilon_z}^e &= \frac{l^e}{n} \cdot \sum_{i=1}^{n} \left(\varepsilon_{z0}(z_i) - \varepsilon_{zo_i}^{\varepsilon}\right)^2 \\
\Phi_{\chi_x}^e &= \frac{I_x^e\, l^e}{A^e\, n} \cdot \sum_{i=1}^{n} \left(\chi_x(z_i) - \chi_{x_i}^{\varepsilon}\right)^2 \\
\Phi_{\chi_y}^e &= \frac{I_y^e\, l^e}{A^e\, n} \cdot \sum_{i=1}^{n} \left(\chi_y(z_i) - \chi_{y_i}^{\varepsilon}\right)^2
\end{aligned} \tag{5}
$$

where l^e, A^e, I_x^e and I_y^e are the length of the element, the area and the moments of inertia with respect to the x and y axes of the section, respectively, n is the number of axial locations where the section strains are evaluated, with coordinates z_i ($0 \leq z_i \leq l^e$). Substituting Eq. (4) in Eq. (1), the analytical section strains are obtained as a function of the nodal degrees of freedom

$$\mathbf{e}(\mathbf{u}) = \mathbf{B}(z) \cdot \mathbf{u}^e \tag{6}$$

where B(z) contains the derivatives of the shape functions. Substituting Eq. (6) in Eq. (5) and then adding all the contributions, yields

$$\frac{\boldsymbol{\Phi}^e}{2} = \frac{1}{2} \cdot \{\mathbf{u}^e\}^T \cdot [\mathbf{S}^e] \cdot \{\mathbf{u}^e\} - \{\mathbf{u}^e\}^T \cdot \{\mathbf{h}^e\} + c$$

where $[S^e]$ is the sum of

$$
\begin{aligned}
\left[\mathbf{S}_{\varepsilon_z}^e\right] &= \frac{l^e}{n} \sum_{i=1}^{n} \left\{\mathbf{B}_{\varepsilon_z}(z_i)\right\}^T \left\{\mathbf{B}_{\varepsilon_z}(z_i)\right\} \\
\left[\mathbf{S}_{\chi_x}^e\right] &= \frac{I_x^e\, l^e}{A^e\, n} \sum_{i=1}^{n} \left\{\mathbf{B}_{\chi_x}(z_i)\right\}^T \left\{\mathbf{B}_{\chi_x}(z_i)\right\} \\
\left[\mathbf{S}_{\chi_y}^e\right] &= \frac{I_y^e\, l^e}{A^e\, n} \sum_{i=1}^{n} \left\{\mathbf{B}_{\chi_y}(z_i)\right\}^T \left\{\mathbf{B}_{\chi_y}(z_i)\right\}
\end{aligned}
$$

and $\{h^e\}$ is the sum of

$$
\begin{aligned}
\left\{\mathbf{h}_{\varepsilon_z}^e\right\} &= \frac{l^e}{n} \sum_{i=1}^{n} \left\{\mathbf{B}_{\varepsilon_z}(z_i)\right\}^T \varepsilon_{zo_i}^{\varepsilon} \\
\left\{\mathbf{h}_{\chi_x}^e\right\} &= \frac{I_x^e\, l^e}{A^e\, n} \sum_{i=1}^{n} \left\{\mathbf{B}_{\chi_x}(z_i)\right\}^T \chi_{x_i}^{\varepsilon}
\end{aligned}
$$

$$\left\{\mathbf{h}^{e}_{\chi_y}\right\} = \frac{I^e_y\, l^e}{A^e\, n} \sum_{i=1}^{n} \left\{\mathbf{B}_{\chi_y}(z_i)\right\}^T \chi^{\varepsilon}_{y_i}$$

Imposing the stationarity of the functional with respect to the kinematic unknowns, the final equation is obtained

$$[\mathbf{S}^e] \cdot \{\mathbf{u}^e\} = \{\mathbf{h}^e\}$$

where the matrix $[S^e]$ depends only on the coordinates of the sensors and on the number of measurements and $\{h^e\}$ contains the input data represented by the experimental strains.

The expansion and assembly of the matrices of the discretized structure, after transformation to a common global reference system, lead to the equation for the whole structure

$$[\mathbf{S}] \cdot \{\mathbf{u}\} = \{\mathbf{h}\}$$

The imposition of the boundary conditions provides a reduced solvable system that allows to obtain the unknown degrees of freedom. The next phase of the formulation involves the derivation of adequate shape functions, consistent with the effective behaviour of the beam, for the interpolation of the displacements. Finally, the procedure for treating strain measurements provided by strain gauges is defined.

4. Element shape functions

In the following, two inverse elements, called 0th and 1st order element, are defined; they are based on the degree of interpolation required as suggested by Eq. (3). In the same way as for the direct finite elements, continuity of order C^{j-1} must be guaranteed on the element interface, where j is the maximum order of derivation of the displacements in the variational formulation. C^1-continuity must be ensured for the deflections whereas C^0-continuity is sufficient for the axial displacement. This interpolation has been realized through the use of Hermite polynomials in terms of non-dimensional coordinates $\xi = (z/l^e) \in [0, 1]$ where $z \in [0, l^e]$ and l^e indicates the element length.

The initial configuration for the 0th order element is characterized by two nodes 1 ($\xi = 0$) and 2 ($\xi = 1$) with ten degrees of freedom (Fig. 3). For the 1st order element, the initial configuration is characterized by 3 nodes 1 ($\xi = 0$), m ($\xi = 1/2$) and 2 ($\xi = 1$) with fourteen degrees of freedom (Fig. 4). This arrangement is reduced to two nodes by eliminating the "internal" degrees of freedom by static condensation, thus obtaining a total of ten degrees of freedom

$$\{\mathbf{u}^e\} = \left\{w_1, v_1, \varphi_{x1}, u_1, \varphi_{y1}, w_2, v_2, \varphi_{x2}, u_2, \varphi_{y2}\right\}^T$$

In this way it is possible to carry out the usual expansion and assembly operations.

4.1 0th order element

This formulation is consistent with the equilibrium conditions for the case of concentrated forces and moments

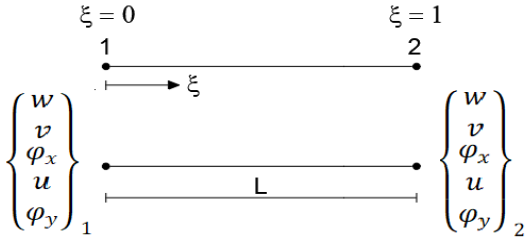

Fig. 3 Two node inverse finite element

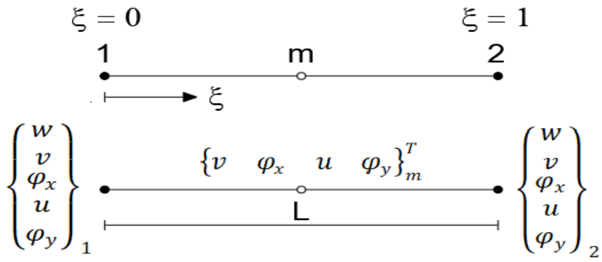

Fig. 4 Initial configuration 1st order element

applied at the end nodes. In this case, the axial and the shear forces are constant along the element whereas the bending moments are linear.

Eq. (2) indicates that the axial deformation ε_{z0} is constant, and the curvatures χ are linear. With reference to Eq. (1), it is deduced that w is linear whereas u and v are cubic. Consequently, the shape functions of w are obtained by considering the Hermite polynomial defined on two nodes ensuring the continuity of the single function, the shape functions of u and v are obtained by considering not only the continuity of the function but also of the derivative. The following set of interpolation relations is obtained

$$w(\xi) = \sum_{i=1}^{2} H^{(0)}_{0i}(\xi) \cdot w_i$$

$$v(\xi) = \sum_{i=1}^{2} H^{(1)}_{0i}(\xi) \cdot v_i + H^{(1)}_{1i}(\xi) \cdot \varphi_{xi}$$

$$u(\xi) = \sum_{i=1}^{2} H^{(1)}_{0i}(\xi) \cdot u_i + H^{(1)}_{1i}(\xi) \cdot \varphi_{yi}$$

where $\mathbf{H}^{(0)}_{0i}$ (i = 1, 2) are the Lagrange linear polynomials and $\mathbf{H}^{(1)}_{ki}$ (i = 1, 2; k = 0, 1) are the cubic Hermite polynomials.

4.2 1st order element

The formulation of the 1st order element is guided by the equilibrium equations for the case of axial forces concentrated at the beam ends and transverse distributed loads $q_y(z)$ and $q_x(z)$.

The substitution of Eq. (1) in Eq. (2), provides the axial displacements remain linear whereas the transverse displacements u and v must be 4th degree polynomials in order to have quadratic curvatures. For this reason, the interpolation of the axial displacement is similar to that of the 0th order element, whereas for the flexural problem it is

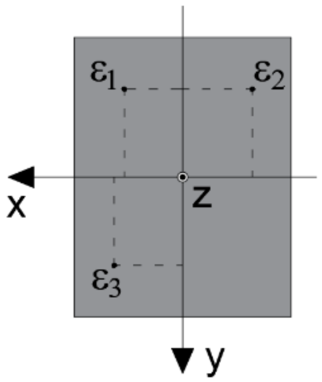

Fig. 5 Strain gauge coordinate system

necessary an interpolation on three points that being of continuity C[1] leads to transverse displacements of the 5th degree. The aforementioned interpolation gives rise to cubic interpolations for χ_x and χ_y; a reduction in degrees of freedom is obtained by imposing a quadratic variation of the curvatures along the element

$$\chi_x = \text{quad.} \qquad \chi_y = \text{quad.}$$

The complete set of displacements results

$$w(\xi) = \sum_{i=1}^{2} H_{0i}^{(0)}(\xi) \cdot w_i$$

$$v(\xi) = Q_{0m}(\xi) \cdot v_m + \sum_{i=1}^{2} Q_{0i}(\xi) \cdot v_i + Q_{1i}(\xi) \cdot \varphi_{xi}$$

$$u(\xi) = Q_{0m}(\xi) \cdot u_m + \sum_{i=1}^{2} Q_{0i}(\xi) \cdot u_i + Q_{1i}(\xi) \cdot \varphi_{yi}$$

where $\mathbf{H}_{0i}^{(0)}$ (i = 1, 2) are coincident with the Lagrange linear polynomials and $\mathbf{Q}_{ki}$ (i = 1, 2; k = 0, 1) are new form of fourth degree shape functions (refer to Appendix A).

Before the further assembly of the global matrix, the degrees of freedom of the central node are eliminated through static condensation, thus simplifying again the topology to two nodes and ten degrees of freedom.

5. Input data from strain gauges

The key phase in the inverse formulation is the usage of the input strain measurements to define the unknown section strains. At each monitored cross section, at least three strain inputs are required in order to completely define the linear axial strain distribution. It should be noted that, in the case of behaviour according to the Timoshenko theroy, at least six input data are required, in order to consider the torsion and shear deformations in the sections (Gherlone *et al.* 2012).

Consider the generic rectangular section at the axial location z (Fig. 5), instrumented with strain gauges at the coordinates x_i and y_i (i = 1, 2, 3).

The equation that relates the axial strains in input and the section strains results

$$\varepsilon_{z,i}^{\varepsilon} = \varepsilon_{z0}^{\varepsilon} + y_i \cdot \chi_x^{\varepsilon} - x_i \cdot \chi_y^{\varepsilon}$$

A further important issue is represented by the minimum number of section strains required within one element, strictly connected to the desired interpolation order and therefore to the type of inverse element chosen.

For the 0th order element, being ε_{z0} constant, χ_x and χ_y linear with respect to the axial coordinate z, five section strain evaluations are necessary at two station points. Similarly, for 1st order element, ε_{z0} is still constant while χ_x and χ_y are quadratic, consequently seven section strain evaluations are necessary at three station points.

6. Implementation and results

In order to test the predictive capacity of the iFEM for the most common cases of civil engineering, some applications for a statically loaded cantilever beam, a simple frame and a continuous beam were considered. The structural elements are made of concrete with Young Modulus E = 30000 MPa and Poisson coefficient = 0.2. The structures were initially analysed with the direct FEM using the LUSAS software with the aim of obtaining the data simulating experimental strain in the required station points (see Figs. 6-8 red dots) and to check the accuracy of the nodal displacements obtained with the iFEM. The structural elements in the LUSAS direct analysis are modelled with Bernoulli-Euler beam elements. The accuracy of the iFEM prediction was assessed by the percentage difference between the predicted displacements and the experimental displacement measurements

$$\%e_{\mathrm{Diff},x} = \frac{x_i^{\mathrm{iFEM}} - x_i^{\mathrm{FEM}}}{x_i^{\mathrm{FEM}}} \cdot 100$$

where “x” indicates the displacement considered.

6.1 Cantilever beam

As first example was considered a cantilever beam with span 3 m and section 0.4 x 1.2 m (slenderness ratio = 2.5). The load conditions applied are concentrated force and distributed load as shown in Fig. 6. In the first case the cantilever beam has been modelled with one 0th order element considering only two station points (z_i = 0.6, 2.4 m), in the second case one 1th order element is considered with three station points (z_i = 0.3, 1.5, 2.7 m).

In Table 1, the percent error for the displacement in y direction of the tip node is reported. Accurate results were obtained for the two load cases with a maximum percent error of less than 1%.

Table 1 Percent error of y displacement of the tip node

Load	Error (%)
F_y	0.0002
q_y	0.0172

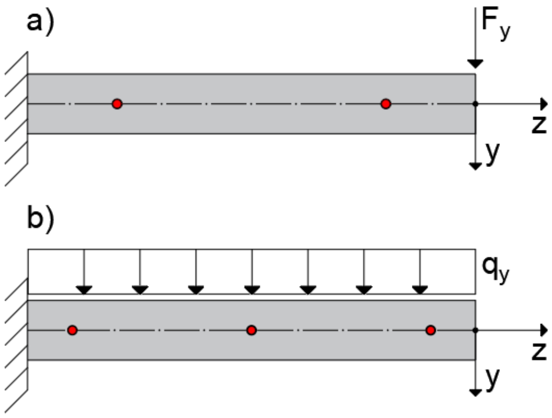

Fig. 6 Cantilever configurations: a) concentrated force with two station points; b) distributed load with three station points

In Fig. 7 the accuracy of the results along the entire length of the element is shown. The green dots indicate the values obtained with the direct FEM in discrete points and the blue line represents the displacements (v) obtained with the iFEM.

6.2 Frame structure

As a second example, the case of a two-dimensional frame loaded with a horizontal force concentrated in node 3 (see Fig. 8) was considered. The considered frame has two levels and it is made up of columns with length of 3 m and section 0.5 x 0.5 m, whereas the beams have span of 5 m and a section of 0.3 x 0.4 m. The segments of the frame were modelled with the 0[th] order element, considering station points at 0.75 m and 2.25 m for the columns and 1.25 m and 3.75 m for the beams (Fig. 8).

In Table 2, the percent error of the axial (w) and transverse (v) displacements of nodes 2, 3, 4 and 5 are reported; furthermore, in this case very satisfactory results have been obtained because the polynomial order in both direct and inverse FEM is the same.

6.3 Continuous beam

In the last case, the continuous beam on four supports and three spans of respectively 30, 40 and 30 m and with a section of 0.5 x 1.7 m was considered. The continuous beam of Fig. 9 is loaded uniformly with distributed load of 50 KN/m and subjected to a couple of moving forces of 150 KN that simulate the effect of the loading tandem system simulating a variable traffic load for road bridges.

In this configuration, further to checking the accuracy of the iFEM for these static conditions, the influence of the two load conditions on the results were analysed. The spans were modelled with the 1[st] order element and a mesh with increasing number of elements (one or two, see Tables 3-4) was considered to observe the effects on the error. The relative positions of the station points for each element are reported in Table 3.

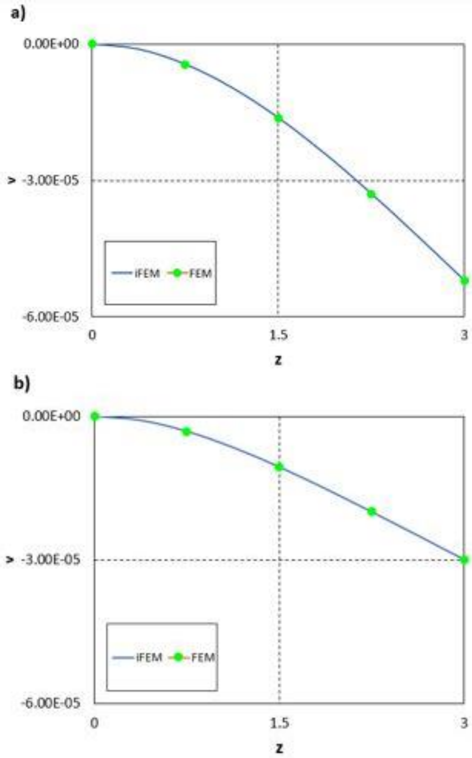

Fig. 7 Transverse displacement v along the z axis for the following cases: a) concentrated force, b) distributed load

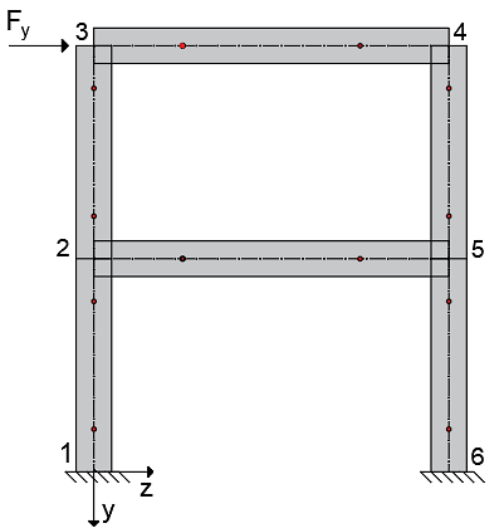

Fig. 8 Two-dimensional frame

Table 2 Percentage of error for nodal displacements

Node	Displacement	Error (%)
2	v	0.0000
	w	0.0001
3	v	0.0000
	w	0.0001
4	v	0.0001
	w	0.0001
5	v	0.0001
	w	0.0001

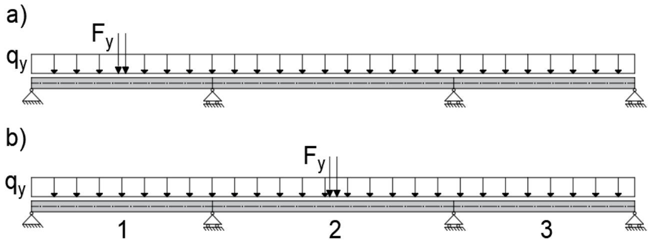

Fig. 9 Loading condition of the continuous beam

Table 3 Position of the station points for each individual element

N. element	Span	Station point (m)
1	1, 3	4.5, 15, 25.5
	2	10, 20, 30
2	1, 3	3, 7.5, 12
	2	6, 10, 14

Table 4 Average percentage error according to the number of elements for span: a) first load condition; b) second load condition

a)

N. element	Span	ERR (%)	$\overline{\text{ERR}}$ (%)
1	1	6.8	2.7
	2	1.0	
	3	0.4	
2	1	0.3	0.3
	2	0.5	
	3	0.1	

b)

N. element	Span	ERR (%)	$\overline{\text{ERR}}$ (%)
1	1	27.1	20
	2	5.7	
	3	27.1	
2	1	1.4	1.1
	2	0.5	
	3	1.4	

The Table 4 shows the average percentage error of the transverse displacement (v). For the two loading cases, it is reported: the number of elements used to mesh each span, the number of spans, the average percentage error for each span calculated averaging every 1.5 m along the span, average percentage error among the three spans.

In this example the iFEM showed a good applicability with respect to the constraint and load conditions, since by modelling each span with just two elements, a maximum error of about 1% in terms of displacements is obtained. For the second load condition, an increase in the percentage error is due to the displacements of a few points close to the bearing characterized by a strong variation in curvature and therefore requiring an increase of mesh in the direct FEM. Unlike the cases of cantilever beam and frame in which the concentrated load was applied to the node of the elements, in the continuous beams, the forces were applied inside the inverse element that was implemented to model quadratic curvature. Due to the discontinuity created by the concentrated loads, an increase in percentage errors can be seen between Table 4 and Tables 2-3. Nevertheless, increasing the number of inverse elements leads to smaller errors.

7. Conclusions

In this paper, a new formulation of the inverse Finite Element Method (iFEM) for the shape sensing of beam and frame structures is presented. The iFEM approach, originally developed by Tessler and Spangler for Mindlin plates and subsequently extended by Gherlone to Timoshenko beams, is here formulated to Bernoulli-Euler beams in order to efficiently analyze civil engineering components and structures.

The basic assumptions of the Bernoulli-Euler beam theory are reviewed and the related formulation of two beam inverse elements is described. The way input data are obtained from measured strains is also addressed. Several example problems (simple beams, frame structures and continuous beams) are presented and discussed in order to assess the accuracy of the developed inverse elements. These are proven to be highly effective and efficient in predicting structural responses and to possess an extreme versatility in terms of structural typology, loading conditions and objectives to be achieved.

Further future efforts of this investigation will be to test the ability of the iFEM not only in the elastic field but also in the presence of cracked elements and to validate the approach with strain data that are affected by measurement noise or that come from experimental measurements.

References

Belabed, Z., Houari, M.S.A., Tounsi, A., Mahmoud, S.R. and Anwar Bég, O.A. (2014), "An efficient and simple higher order shear and normal deformation theory for functionally graded material (FGM) plates", *Compos. Part B*, **60**, 274-283. https://doi.org/10.1016/j.compositesb.2013.12.057.

Akl, W., Poh, S. and Baz, A. (2007), "Wireless and distributed sensing of the shape of morphing structures", *Sensors Actuators,* **140**, 94-102. https://doi.org/10.1016/j.sna.2007.06.026.

Cerracchio, P., Gherlone, M. and Tessler, A. (2015a), "Real-time displacement monitoring of a composite stiffened panel subjected to mechanical and thermal loads", *Meccanica,* **50**(10), 2487-2496. https://doi.org/10.1007/s11012-015-0146-8.

Cerracchio, P., Gherlone, M., Di Sciuva, M. and Tessler, A. (2015b), "A novel approach for displacements and stress monitoring of sandwich structures based on the inverse Finite Element Method", *Compos. Struct.*, **127**, 69-76. https://doi.org/10.1016/j.compstruct.2015.02.081.

Gherlone, M. (2008), "Beam inverse finite element formulation", Research Report No. 1; Department of Aeronautics and Space Engineering, Politecnico di Torino, Torino, Italy.

Gherlone, M., Cerracchio, P., Mattone, M., Di Sciuva, M. and Tessler, A. (2012), "Shape sensing of 3D frame structures using an inverse Finite Element Method", *J. Solid. Struct.,* **49**, 3100-

3112. https://doi.org/10.1016/j.ijsolstr.2012.06.009.

Gherlone, M., Cerracchio, P., Mattone, M., Di Sciuva, M. and Tessler, A. (2014), "An inverse finite element method for beam shape sensing: theoretical framework and experimental validation", *Smart Mater. Struct.*, **23**(4), 045027. https://doi.org/10.1088/0964-1726/23/4/045027.

Gherlone, M., Cerracchio, P. and Mattone, M. (2018), "Shape sensing methods: review and experimental comparison on a wing-shaped plate", *Progress Aerosp. Sci.,* **99**, 14-26. https://doi.org/10.1016/j.paerosci.2018.04.001.

Glaser, R., Caccese, V. and Shahinpoor, M. (2012), "Shape monitoring of a beam structure from measured strain or curvature", *Exp. Mech.,* **52**, 591–606. https://doi.org/10.1007/s11340-011-9523-y.

Henault, J.M., Quiertant, M., Delepine-Lesoille, S., Salin, J., Moreau, G., Taillade, F. and Benzarti, K. (2012), "Quantitative strain measurement and crack detection in RC structures using a truly distributed fiber optic sensing system", *Construct. Build. Mater.,* **37**, 916-923. https://doi.org/10.1016/j.conbuildmat.2012.05.029.

Hong-Hu, Z., Jian-Hua, Y., Lin, Z., Wei, J. and Jian-Hua, D. (2009), "Monitoring internal displacements of a model dam using FBG sensing bars", *Adv. Struct. Eng.,* **13**, 249-261. https://doi.org/10.1260/1369-4332.13.2.249.

Jiang, T., Shen, Z., Yang, M., Xu, L., Gan, L. and Cui, X. (2018), "A new model approach to predict the unloading rock slope displacement behaviour based on monitoring data", *Struct. Eng. Mech.*, **67**(2), 105-113. https://doi.org/10.12989/sem.2018.67.2.105.

Ju, M., Park, K., Moon, D., Park, C. and Sim, J. (2018), "On strain measurement of smart GFRP bars with built-in fiber Bragg grating sensor", *Struct. Eng. Mech.*, **65**(2), 155-162. https://doi.org/10.12989/sem.2018.65.2.155.

Kefal, A., Oterkus, E., Tessler, A. and Spangler, J.L. (2016a), "A quadrilateral inverse-shell element with drilling degrees of freedom for shape sensing and structural health monitoring", *Eng. Sci. Tehcnol.,* **19**(3), 1299-1313. https://doi.org/10.1016/j.jestch.2016.03.006.

Kefal, A. and Oterkus, E. (2016b), "Displacement and stress monitoring of a chemical tanker based on inverse finite element method", *Ocean Eng.,* **112**, 33-46. https://doi.org/10.1016/j.oceaneng.2015.11.032.

Kefal, A. and Oterkus, E. (2016c), "Displacement and stress monitoring of a Panamax containership using inverse finite element method", *Ocean Eng.*, **119**, 16-29. https://doi.org/10.1016/j.oceaneng.2016.04.025.

Kefal, A., Mayang, B.J., Oterkus, E. and Yildiz, M. (2018), "Three dimensional shape and stress monitoring of bulk carriers based on iFEM methodology", *Ocean Eng.*, **147**, 256-267. https://doi.org/10.1016/j.oceaneng.2017.10.040.

Kefal, A., Tessler, A. and Oterkus, E. (2017a), "An enhanced inverse finite element method for displacement and stress monitoring of multi-layered composite and sandwich structures", *Compos. Struct.*, **179**, 514-540. https://doi.org/10.1016/j.compstruct.2017.07.078.

Kefal, A. and Yildiz, M. (2017b), "Modeling of sensor placement strategy for shape sensing and Structural Health Monitoring of a wing-shaped sandwich panel using inverse Finite Element Method", *Sensors*, **17**(12), 2775. https://doi.org/10.3390/s17122775.

Kim, N.S. and Cho, N.S. (2004), "Estimating deflection of a simple beam model using fiber optic Bragg-grating sensors", *Exp. Mech.,* **44**, 433-439. https://doi.org/10.1007/BF02428097

Kirby, G.C., Lim, T.W., Weber, R., Bosse, A., Povich, C. and Fisher, S. (1997), "Strain based shape estimation algorithms for cantilever beam", *Proceedings of SPIE* 3041, San Diego, California, June.

Ko, W.L., Richards, W.L. and Fleischer, V.T. (2009), "Applications of Ko displacement theory to the deformed shape predictions of the doubly-tapered Ikhana wing", NASA/TP 214652, 01 October, California.

Mao, Z. and Todd, M. (2008), "Comparison of shape reconstruction strategies in a complex flexible structure", *Proceedings of SPIE* 6932, San Diego, California, April.

Papa, U, Russo S., Lamboglia, A., Del Core, G. and Iannuzzo, G. (2017), "Health structure monitoring for the design of an innovative UAS fixed wing through inverse finite element method", *Aerosp. Sci. Technol.,* **69**, 439-448. https://doi.org/10.1016/j.ast.2017.07.005.

Quiertant, M., Baby, F., Khadour, A., Marchand, P., Rivillon, P., Billo, J., Lapeyrere, R., Toutlemonde, F., Simon, A. and Cordier, J. (2013), "Deformation monitoring of reinforcement bars with a distributed fiber optic sensor for the SHM of reinforced concrete structures", *Seventh International Conference on Concrete under Severe Conditions – Environment and Loading,* China, September.

Regier, R. and Hoult, N.A. (2014), "Distributed strain behaviour of a reinforced concrete bridge: Case study", *J. Bridge Eng.,* **19**(12), 1-9. https://doi.org/10.1061/(ASCE)BE.1943-5592.0000637.

Rodríguez, G., Casas, J.R., Villalba, S. and Barrias, A. (2016), "Monitoring of shear cracking in partially prestressed concrete beams by distributed optical fiber sensors", *Proceedings of the 8th International Conference on Bridge Maintenance, Safety and Management,* Foz do Iguaçu, Brazil, June.

Serker, N.H.M. and Wu, Z.S. (2010), "Structural health monitoring using static and dynamic strain data from long-gage distributed FBG sensor", *Joint Conference on Advances in Bridge Engineering-II,* Dhaka, Bangladesh, August.

Shi, B., Sui, H., Liu, J. and Zhang, D. (2009), "The BOTDR-based distributed monitoring system for slope engineering", *Proceedings of the 10th IAEG International Congress,* Nottingham, UK, January.

Shi, B., Xu, H., Chen, B., Zhang, D., Ding, Y., Cui, H. and Gao, J. (2003), "A Feasibility Study on the Application of Fiber-Optic Distributed sensors for strain measurement in the Taiwan strait tunnel project", *Marine Georesources and Geotechnology,* **21**, 333–343. https://doi.org/10.1080/713773406.

Shkarayev, S., Krashantisa, R. and Tessler, A. (2001), "An inverse interpolation method utilizing in-flight strain measurements for determining loads and structural response of aerospace vehicles", *Proceedings of the 3rd International Workshop on Structural Health Monitoring,* Stanford, California.

Tessler, A. and Spangler, J.L. (2003), "A variational principle for reconstruction of elastic deformation of shear deformable plates and shells", NASA TM-2003-212445; NASA Langley Research Center; Hampton, VA, USA.

Tessler, A. and Spangler, J.L. (2004), "Inverse FEM for full-field reconstruction of elastic deformations in shear deformable plates and shells", *2nd European Workshop on Structural Health Monitoring,* Munich, Germany.

Thévenaz, L., Facchini, M., Fellay, A., Robert, P., Inaudi, D. and Dardel, B. (1999), "Monitoring of large structure using distributed Brillouin fibre sensing", *Proceedings of the 13th International Conference on Optical Fiber Sensors,* Kyongju, Korea, April.

Tondolo, F., Cesetti, A., Matta, E., Quattrone, A. and Sabia, D. (2018), "Smart reinforcement steel bars with low-cost MEMS sensors for the structural health monitoring of RC structures", *Construct. Build. Mater.,* **173**, 740-753. https://doi.org/10.1016/j.conbuildmat.2018.04.045.

Unsal, I., Tokgoz, S., Cagatay, H.I. and Dundar, C. (2017), "A study on load-deflection behaviour of two-span continuous concrete beams reinforced with GFRP and steel bars", *Struct. Eng. Mech.*, **63**(5), 629-637. https://doi.org/10.12989/sem.2017.63.5.629.

Villalba, S. and Casas, J.R. (2012), "Application of optical fiber distributed sensing to health monitoring of concrete structures", *Mech. Syst. Signal Process.,* **39**, 441-451. https://doi.org/10.1016/j.ymssp.2012.01.027.

Zeng, X., Bao, X., Chhoa, C.Y., Bremner, T.W., Brown, A.W., DeMerchant, M.D., Ferrier, G., Kalamkarov, A.L. and Georgiades, A.V. (2002), "Strain measurement in a concrete beam by use of the Brillouin-scattering-based distributed fiber sensor with single-mode fibers embedded in glass fiber reinforced polymer rods and bonded to steel reinforcing bars", *Appl. Optics,* **41**, 5105-5114. https://doi.org/10.1364/AO.41.005105.

CC

Appendix A

The interpolation of the transverse displacements for the 1st order element is obtained by imposing constraints on the variation of the curvatures along the extension of the element. In particular, the curvatures must be quadratic. From the 1st order Hermite polynomials defined on 3 points (1, m, 2), the transverse displacements are given by the following interpolation scheme

$$\begin{aligned} v(\xi) &= \sum_{i=1}^{1,m,2} H_{0i}(\xi) \cdot v_i + H_{1i}(\xi) \cdot \varphi_{xi} \\ u(\xi) &= \sum_{i=1}^{1,m,2} H_{0i}(\xi) \cdot u_i + H_{1i}(\xi) \cdot \varphi_{yi} \end{aligned} \tag{7}$$

where $\mathbf{H}_{ki}$ (i = 1, m, 2; k = 0, 1) are the Hermite polynomials of fifth degree. Substituting these terms in the expressions of the curvature gives rise to cubic polynomials

$$\begin{aligned} \chi_x &= -\sum_{i=1}^{1,m,2} H_{0i,\xi\xi}(\xi) \cdot v_i + H_{1i,\xi\xi}(\xi) \cdot \varphi_{xi} \\ \chi_y &= \sum_{i=1}^{1,m,2} H_{0i,\xi\xi}(\xi) \cdot u_i + H_{1i,\xi\xi}(\xi) \cdot \varphi_{yi} \end{aligned} \tag{8}$$

The reduction of the polynomial order from cubic to quadratic is obtained by imposing the vanishing of all the cubic terms contained in the equations (8).

$$\frac{480}{L} v_1 - 80\varphi_{x1} - 320\varphi_{xm} - \frac{480}{L} v_2 - 80\varphi_{x2} = 0$$

$$\frac{480}{L} u_1 - 80\varphi_{y1} - 320\varphi_{ym} - \frac{480}{L} u_2 - 80\varphi_{y2} = 0$$

The previous equations can be solved for the two internal degrees freedom, φ_{xm} and φ_{ym}. Then, replacing φ_{xm} and φ_{ym} in the equations (7), the final interpolation for the deflections v and u is obtained.